A chromatic nanoswitcher for thermal monitoring of cell metabolism

Fengchan Zhang, Marina París Ogáyar, Álvaro Artiga, Jordi Hernando, Eva Villar-Álvarez, Julia Lorenzo, Beñat Salegi Ansa, Sara Cogliati, Laura Formentini, Patricia Haro-González, Daniel Ruiz-Molina, Jaume Ramon Otaegui, Claudio Roscini,* and Daniel Jaque**

F. Zhang, M. París Ogáyar, Á. Artiga, P. Haro-González, D. Jaque
Nanomaterials for Bioimaging Group (nanoBIG), Departamento de Física de Materiales, Facultad de Ciencias, Universidad Autónoma de Madrid, Madrid 28049, Spain
E-mail: daniel.jaque@uam.es

F. Zhang, P. Haro-González
Instituto Nicolás Cabrera, Facultad de Ciencias, Universidad Autónoma de Madrid, Madrid 28049, Spain

J. Hernando, J. R. Otaegui,
Departament de Química, Universitat Autònoma de Barcelona, Edifici C/n, Campus UAB, Cerdanyola del Vallès 08193, Spain
E-mail: jaume@wustl.edu

E. Villar-Álvarez, D. Ruiz-Molina, C. Roscini
Catalan Institute of Nanoscience and Nanotechnology (ICN2), CSIC and BIST, Campus UAB, Bellaterra, Barcelona 08193, Spain
E-mail: claudio.roscini@icn2.cat

J. Lorenzo
Institut de Biotecnologia i Biomedicina, and Departament de Bioquímica i Biologia Molecular, Universitat Autònoma de Barcelona, Cerdanyola del Vallès, 08193, Barcelona, Spain
Centro de Investigación Biomédica en Red: Bioingeniería, Biomateriales y Nanomedicina, 08193, Cerdanyola del Vallès, Spain,

B. Salegi Ansa, S. Cogliati, L. Formentini
Facultad de Ciencias, Departamento de Biología Molecular, Centro de Biología Molecular ‘“Severo Ochoa’” (CBM, UAM-CSIC), c/ Nicolás Cabrera 1, Universidad Autónoma de Madrid, Madrid 28049, Spain.

B. Salegi Ansa, L. Formentini
Instituto de Investigación Hospital 12 de Octubre, i+12, Madrid 28049, Spain.

P. Haro-González, D. Jaque
Institute for Advanced Research in Chemical Sciences, Facultad de Ciencias, Universidad Autónoma de Madrid, Madrid, 28049, Spain

D. Jaque
Nanomaterials for Bioimaging Group (nanoBIG), Instituto Ramón y Cajal de Investigación Sanitaria (IRYCIS), Hospital Ramón y Cajal, Madrid 28034, Spain

Keywords: nanothermometry, intracellular temperature, phase change material, silica nanocapsules, cellular metabolism

Abstract:

Accurate sensing of intracellular temperature is crucial for understanding and monitoring cell metabolism, serving as an initial step toward diagnosing conditions such as mitochondria-related diseases. However, thermal monitoring of cell metabolism is challenging due to the minimal temperature variations caused by intracellular metabolic activity (typically around 1 °C) and by the risk of crosstalk in intracellular sensors. We present a novel type of intracellular thermal sensor based on silica nanocapsules filled with a thermo-responsive fluorescent medium. This medium undergoes a reversible phase transition from solid to liquid at temperatures around 37 °C, inducing a chromatic switch that facilitates remote thermal sensing. Our chromatic switchers exhibit a thermal sensitivity of approximately 13 % $°C^{-1}$ at 37 °C, one of the highest reported for intracellular thermal sensing. Notably, the thermal response is unaffected by external factors such as pH, ionic strength, and viscosity. Moreover, we confirm that the response of our sensors is not affected by the cellular activity, underscoring their reliability for cytoplasmic temperature measurements. We finally demonstrate the potential of these sensors by measuring intracellular heating during the metabolic switch from mitochondrial to glycolytic activity, showcasing their potential for real-time, precise thermal monitoring (< 1 ºC) of cell metabolism.

1. Introduction

Understanding the intricacies of cellular dynamics requires precise tools capable of real-time temperature monitoring within the complex milieu of living systems. Temperature fluctuations are integral indicators of cellular metabolism, influencing various biochemical processes crucial for cell function.[1-3] Unfortunately, assessing the internal temperature of a live cell is as interesting as challenging. On one hand, temperature changes inside cells caused by, for instance, metabolic activity, are of few tenths of Celsius degrees. In addition, intracellular temperature sensing must be achieved remotely to minimally perturb the cell's intrinsic behavior.

Luminescent nanothermometers (LNThs) appeared as promising tools for remote and accurate intracellular temperature measurement.[4-6] LNThs are nanoparticles or molecules whose luminescence is strongly affected by the environmental temperature.[7-9] A proper analysis of the luminescence generated by LNThs within cells allows, in principle, for a remote thermal readout of intracellular temperature. LNThs have already been used for thermal monitoring of different intracellular processes such as chemical shocks,[10, 11] photothermal therapies[12] and, even, metabolic activation[13] and suppression.[14] The working procedure for intracellular thermal sensing by using LNThs is quite simple: the thermal response of the LNThs is first measured in solution to build a calibration curve: Δ vs T curve, where Δ is the spectroscopic parameter used for temperature determination. Then LNThs are incorporated into cells and their emitted luminescence is recorded and analyzed to find the value of Δ. Finally, the use of the calibration curve allows us to translate the intracellular value of Δ into intracellular temperature. This simple procedure is based on the premise that the thermal response of LNThs within cells is the same as in solution and that the spectroscopic parameter Δ does only depend on temperature and not on other physico-chemical parameters that fluctuate in the intracellular medium together with temperature (viscosity, ionic strength, pH, etc...). These two premises are not always satisfied. Indeed, the reliability of intracellular temperature measurements provided by LNThs have been questioned as several LNThs show different responses in solution or within cells.[15-17] This could happen when temperature is not the only parameter affecting the luminescence of LNThs but, instead, the physico-chemical properties of cytoplasm and/or the intrinsic cell activity also modify the thermometric parameter Δ. The presence of crosstalk or bias has cast doubt on the accuracy of temperature readings obtained using conventional LNThs, highlighting the urgent need for new luminescent nanomaterials whose

thermal response would be completely independent on variations in the physio-chemical properties of surrounding medium.[18]

In this paper, we present a step forward to reliable intracellular thermal sensing through the synthesis and application of a novel class of LNThs. Our LNThs are constituted by a silica spherical shell filled with a thermoresponsive medium containing a fluorescent dye. The silica shell provides mechanical stability to the structure and minimizes the interaction of fluorescent medium with environment. The thermoresponsive medium undergoes a phase transition in the physiological temperature range that causes a thermally induced change in the luminescence color generated by the dye, so that the whole structure behaves as a chromatic nanoswitcher (ChNS). The spectral analysis of emission spectra of our ChNS can be used for precise temperature determination. The presence of this silica shell together with the hydrophobic character of the medium/dye mixture results in a negligible impact of the physico-chemical properties of intracellular medium on the thermal response of our ChNS. This distinctive characteristic addresses the critical limitation of some of the previously used LNThs, where their thermal properties diverge between solution and cellular contexts, leading to inaccuracies in temperature measurements. The actual potential of our phase transition (PT)-based LNThs has been proved by evaluating their capability to monitor cellular temperature dynamics during the activation of cellular metabolism.

2. Results and discussion

2.1. Synthesis and characterization of chromatic nanoswitchers

For the preparation of our silica nanocapsules, we employed a mixture of the paraffins eicosane (EC, T_m = 36.5 ºC) and docosane (DC, T_m = 42-45 ºC)[19] as thermoresponsive medium (1:1 weight ratio), and *N*,*N*'-bis(1-hexylheptyl)perylene-3,4,9,10-bis(dicarboximide) (PDI) as a fluorescent dye. The rationale to use this EC-DC mixture is that such combination leads to a reduction in the sharpness of the phase transition so that it is produced all along the physiological range of interest for intracellular measurements (35-42 ºC). Details of the synthesis are reported in the experimental section. Although PDI fluorescence is not intrinsically thermoresponsive, it can be reversibly switched between excimer/aggregate red emission and monomeric green fluorescence upon dissolution in phase changing paraffins. By taking advantage of the different solubility of the dye in the solid and liquid states of

paraffins, PDI molecular aggregation/disaggregation and, therefore, red-green emission modulation can

be promoted through the thermally-induced phase transition of the surrounding medium (**Figure 1a**), a behavior that we have already exploited for optical device fabrication (e.g., security inks, data encoding).[20-22] The final ChNSs resulted of around 51 nm in diameter (**Figures 1b and Figure S1**) and exhibited a clear core-shell structure, as shown by both transmission electron microscope (TEM) and energy dispersive X-Ray (EDX) elemental mapping images (**Figures 1b-c**). The presence of the paraffin-based thermoresponsive medium inside the ChNS nanocapsules was corroborated by differential scanning calorimetry, which shows a solid-to-liquid transition starting at T = 36.5 ºC (**Figure S2**).

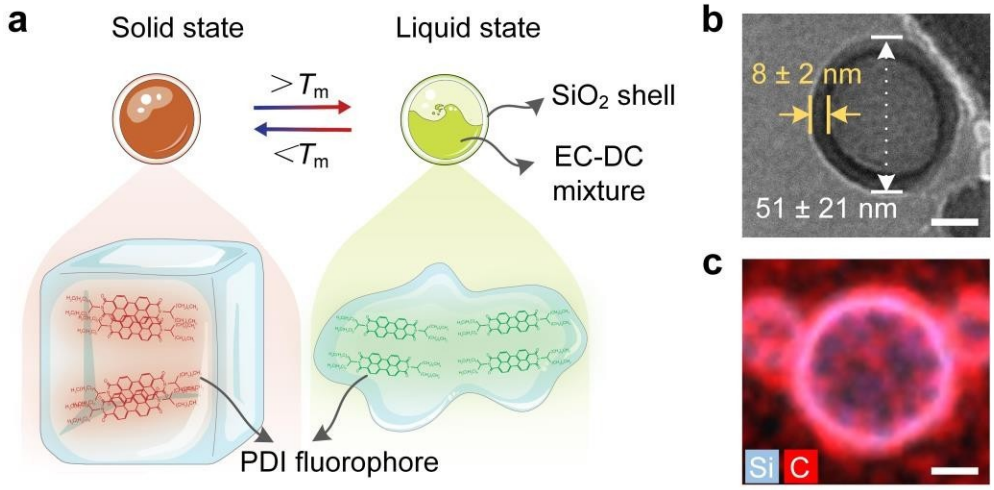

Figure 1. (a) Schematic illustration of the ChNSs based on silica nanocapsules, which are loaded with an EC-DC (1:1 weight ratio) mixture containing the PDI fluorophore dissolved. The solid-to-liquid transition induces the aggregation-disaggregation process of the dye and the consequent emission color change, from red to green. T_m: melting point of the EC-DC mixture.

(b) One representative TEM image of the ChNS. Note that the sizes presented here represent the mean ± S. D. from more than 500 silica nanocapsules. **(c)** EDX elemental maps of silica (blue) and carbon (red). Scale bars: 20 nm.

2.2. Thermal calibration and reliability of chromatic nanoswitchers in aqueous solutions

The fluorescence properties of our ChNSs were first calibrated by recording their emission in an aqueous suspension under 405 nm excitation in the 25-60 ˚C temperature range (**Figure 2**). As the temperature increases, a switch of the emission color and spectrum is observed because of the phase transition that starts at T_{PT} = 36.5 ºC. For temperatures below 36.5 ºC, the medium within the silica shell is in its solid phase, and the selective aggregation of the dye

molecules that occurs in the solid state of the system leads to a broadband red emission band with its maximum at around 650 nm (**Figure 2a** and **Figure 2c**). As temperature increases above 36.5

ºC, the onset of the melting of the PT medium takes place (as also corroborated by differential scanning calorimetry measurements of the capsules, **Figure S2**) and dye molecules start to disaggregate, thereby leading to the characteristic well-structured green luminescence of PDI monomers (**Figure 2b** and **Figure 2c**). The relative contribution of this green band to the overall emission increases with temperature due to the progressive melting of the paraffin medium and/or the progressive dissolution of the PDI in the liquid paraffin mixture. For temperatures above 42 ºC the luminescence generated by our ChNSs is mainly constituted by this green band in agreement with an almost complete melting of the inner medium.

To exploit the chromatic switching of our ChNSs for thermal sensing, we defined the green-to- red emission intensity ratio (R_{gr}) as a thermometric parameter. $R_{gr} = I_g / I_r$ is calculated by dividing the integrated luminescence intensity into two complementary spectral regions covering most of the PDI monomer and aggregate emission, 515-600 nm (I_g) and 600-790 nm (I_r). The rationale behind the selection of these spectral ranges is described in **Section 3**, **Supporting Information** (**Figure S3**). In accordance with the drastic change of emission spectra with temperature (**Figure 2c**), R_{gr} shows a strong temperature dependence (**Figure 2d**). For temperatures below 32 ºC the intensity ratio is almost temperature independent ($R_{gr} \cong 0.2$). For temperatures in the 32-42 ºC range R_{gr} becomes highly dependent on temperature due to the progressive melting of the paraffin filling of our ChNSs. Finally, for temperatures above 42 ºC R_{gr} reduces its temperature dependence in accordance with a complete melting of paraffin filling. Although with different rates, R_{gr} increases with temperature in the whole temperature range studied. This means that there are not two temperatures leading to the same intensity ratio and that R_{gr} can be used for unequivocal determination of the temperature of the ChNSs. The

thermal sensitivity of our ChNSs, defined as $S_r = R_{gr}^{-1} \cdot dR_{gr}/dT$, reaches a maximum of 26 %·ºC^{-1} at 37 ºC, which lies among the highest thermal sensitivities reported for ratiometric LNThs (see **Table S1** in **Supporting Information**). Noticeably, although maximum sensitivities are achieved in the 32-42 ºC range, our ChNSs also show non-vanishing thermal sensitivities for temperatures below 32 ºC and above 42 ºC. Therefore, they can be also used in these other thermal ranges (although they will provide less precise thermal readouts). The

high thermal sensitivity at 37 ºC is achieved without any luminescence quenching. Indeed, the total (I_g + I_r) luminescence intensity generated is not thermally quenched but, instead, it increases moderately (+35 %) during the chromatic switching. This is an advantage over other ChNSs that show relevant (-60 %) thermal quenching around 37 ºC (**Figure S4**).[23] There are different reasons why our ChNSs exhibit non-thermal fluorescence quenching. First of all, they were

designed to switch with temperature between two different emitting species: PDI excimers at low temperatures and PDI monomers at higher temperatures, both of which are known to present high fluorescence quantum yields when dispersed in phase change materials.[21] In addition, because the fluorescence quantum yield of PDI monomers is even higher than that of PDI excimers, the fluorescence intensity of our ChNSs slightly increases when heating above the melting point of the EC-DC mixture instead of decreasing (see **Figure S4a**, **Supporting Information**). Finally, once the PDI excimer species are fully converted into the PDI monomer at high temperatures, the fluorescence of the latter remains constant despite further heating, a behavior that is expected due to the low temperature-dependence of emission quantum yield for rigid polyaromatic dyes.[24] Since the precision of thermal readouts depend on the signal-to- noise ratio of emitted intensities,[25] the absence of any thermal quenching in our ChNSs ensures a precise thermal reading in the whole physiological range.

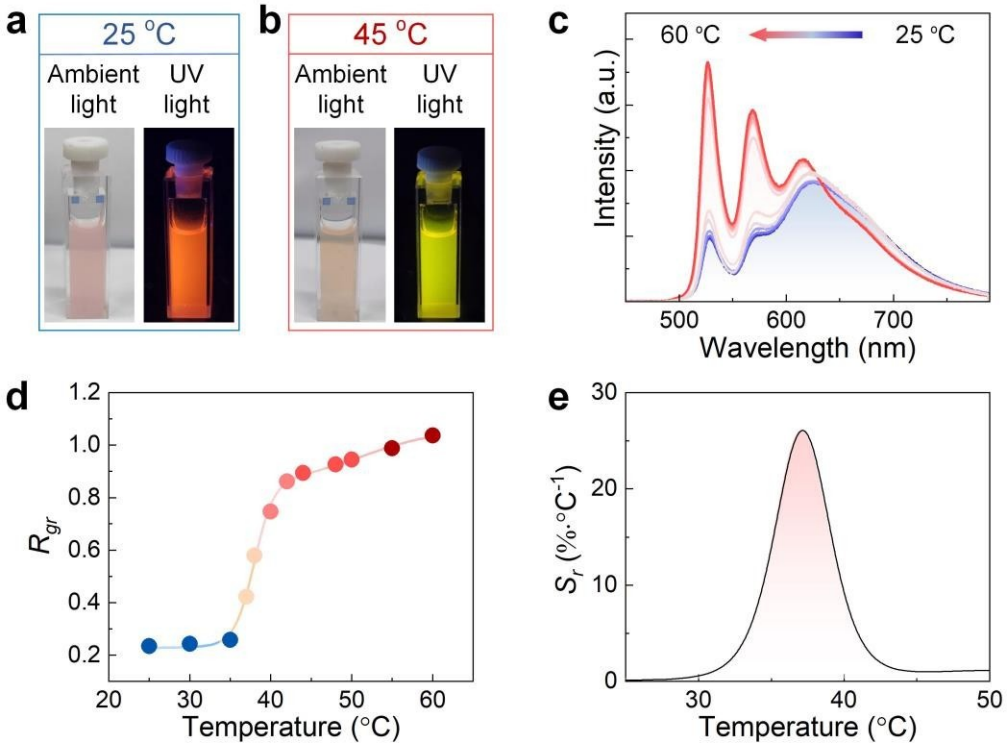

Figure 2. Photographs of a colloidal suspension of ChNSs under ambient light and UV light (λ_{exc} = 365 nm) as obtained at **(a)** 25 ºC and **(b)** 45 ºC. **(c)** Emission spectra registered for an aqueous suspension of ChNSs at different temperatures. Excitation wavelength was 405 nm. **(d)** Temperature dependence of the intensity ratio R_{gr} for the emission of ChNSs suspended in water. Symbols are experimental data, and the solid line is the best fitting to a *biphasic-dose response* function. $y = 0.23 + [0.62/(1.0 + 2.3 * 10^{(38-x)})] + [0.21/(1.0 + 7.5 *$

$10^{(51-x)})]$, $R^2 = 0.998$. **(e)** Temperature dependence of the relative thermal sensitivity S_r calculated from data shown in **(d)**.

The robustness of our ChNSs was first evaluated by subjecting them to consecutive heating and cooling cycles. The temperature chromatic switching behavior measured throughout these cycles was reproducible and no significant variation was observed for the amplitude of the temperature-induced change in R_{gr} (**Figure 3a**). In addition, the continuous irradiation of our ChNSs under 405 nm laser for prolonged time did not induce changes in the thermometric parameter R_{gr} – i.e., they are highly photostable (**Figure 3b**). Furthermore, the R_{gr} vs T curves corresponding to our ChNS dispersed in aqueous solution were found to be unaffected when tested in different conditions of relevance for biological environments: pH (**Figure 3c**), viscosity (**Figure 3d**), KCl concentration (**Figure 3e**), and presence/absence of glucose (**Figure 3f**). Thus, we can state that the thermometric parameter R_{gr} provided by ChNSs in aqueous suspensions does only depend on temperature and the thermal readouts achieved from its experimental evaluation would be reliable and free from bias. This is an advantage over other LNThs, such as fluorescent proteins, used for intracellular thermal sensing in which their spectroscopic properties were also affected by the physical-chemical properties of surrounding medium.[15] **Figure 3** supports the potential use of our ChNSs for reliable and remote intracellular thermal sensing although their actual performance within cells needs to be explored.

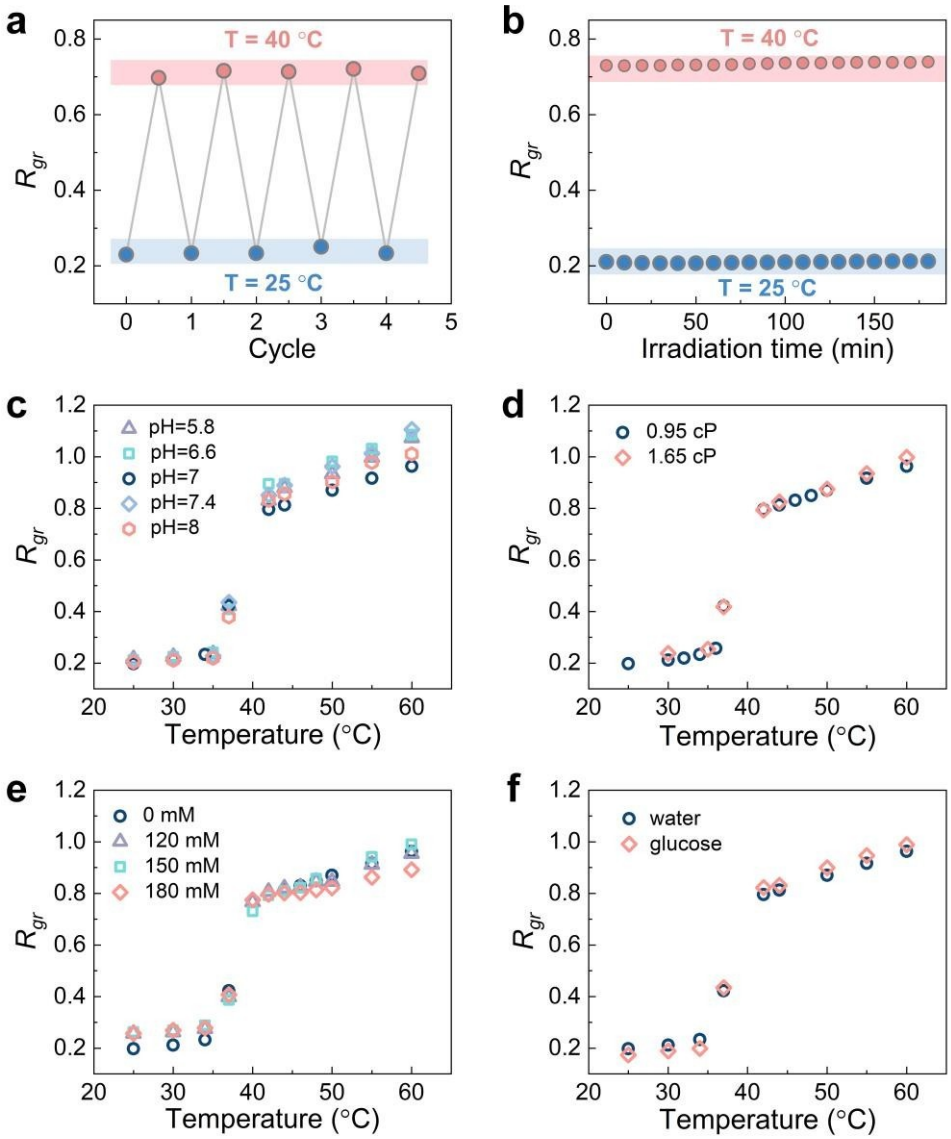

Figure 3. **(a)** Intensity ratio R_{gr} corresponding to an aqueous suspension of ChNSs at 25 and 40 °C as obtained after consecutive heating and cooling cycles. **(b)** Time evolution of the intensity ratio R_{gr} corresponding to an aqueous suspension of ChNSs under continuous irradiation of 405 nm laser. Data obtained at 25 and 40 ºC are included. R_{gr} vs T curves corresponding to ChNSs dispersed in aqueous media for different values of **(c)** pH, **(d)** viscosities, concentrations of **(e)** KCl, and **(f)** glucose contents.

2.3. Intracellular response of chromatic nanoswitchers

Although data of **Figure 3** suggest that the thermal response of our ChNSs would be reliable in any environmental conditions, their reliability as intracellular thermal sensors needs to be corroborated by *in vitro* studies. Cytoplasm is a complex system in which mechanical and chemical conditions change dynamically due to the presence of cell activity. In addition, these

changes affect multiple parameters at the same time, so the fact that the thermal response of our ChNSs is not affected by single-parameter variations (**Figure 3**) does not ensure that they would still behave as reliable thermal sensors within cells. To elucidate this question, we incubated Uppsala 87 malignant glioblastoma (U87-MG) cells with our ChNSs. Fluorescence images revealed the co-localization of ChNSs and U87-MG cells (**Figure 4a**). In addition, 3D scanning confocal microscopy confirms the intracellular location of the ChNSs (**Figure 4b**) probing that they were internalized by the cells. The ChNSs displays low cytotoxicity to the cells (ca. viability of 90% at a concentration up to 200 μg mL^{-1}, **Figure S5**).

The thermal response (chromatic switching) of our ChNSs within live cells was investigated by placing the U87-MG cells on a temperature-controlled microscope stage mechanically attached to the fluorescence microscope. A broad-band blue LED (415-500 nm) was used to excite the ChNSs within cells. By using a filter selector, we recorded the fluorescence images of the live U87-MG cells in two spectral ranges: Green: 515-600 nm, and Red: 600-790 nm (**Figure 4c**). The pixel-by-pixel intensity division of the later (Red) by the former (Green) images results in a R_{gr} cell image (ratiometric image, **Figure 4d**). As it occurs in aqueous suspensions, the solid- to-liquid phase transition of the PT medium induces the red-to-green fluorescence switch of the intracellularly located ChNSs (**Figure 4e**). For the sake of comparison, we also include in **Figure 4e** the temperature variation of R_{gr} corresponding to ChNSs in absence of cells measured with the same fluorescence microscope. The thermal response of ChNSs is found to be, within experimental uncertainty, identical in absence and presence of cells. Here the thermal response refers to the temperature at which the chromatic switching occurs, rather than the absolute R_{gr}. In some cases, differences in cell lines or experimental conditions (e.g., measurement duration or the volume of culture medium) may cause the temperature of live cells to differ from that of the medium, leading to a variation in R_{gr} when measured in absence or presence of cells. Such differences were not significant in our experiments. In any case, our results indicate that the presence or absence of cellular metabolism has not any impact on the thermal response of our ChNSs. This last feature constitutes an advantage over other intracellular thermal sensors (such as fluorescence proteins and semiconductor quantum dots) whose response has been reported to be significantly affected by cell metabolism.[15]

A detailed comparison between the R_{gr} vs T curves obtained from the analysis of fluorescence images or emission spectra (**Figure 4e** and **Figure 2d**, respectively) shows the same fluorescent switching temperature, T = 36.5 ºC. On the other hand, the comparison between

Figure 4e and **Figure 2d** revealed different modulation depths for R_{gr} depending on the experimental setup

used to measure the chromatic switch: R_{gr} varies from 0.2 to 0.9 in **Figure 2d** (data corresponding to an aqueous suspension measured with a spectrometer), while R_{gr} increases from 0.7 up to 1.6 when measured with the fluorescence microscope (**Figure 4e**). We attribute the different values of R_{gr} to the different procedures used in each case for the calculation of R_{gr}, the different excitation source, and the different spectral response of the spectrum analyzer and the fluorescence camera. We state that similar differences have been reported in previous works dealing with the calibration of optical sensors using different experimental setups. [10, 23, 26, 27]

Data of **Figure 4** allow concluding that the luminescence properties of our ChNSs are not affected by neither the intracellular presence of organelles nor by the changes in the physico-chemical properties of cytoplasm that could be caused by the intrinsic cell activity. Indeed, **Figure 4** reveals that in the 33-42 °C temperature range there is an unequivocal relation between R_{gr} and the cell temperature. In other words, in this spectral range our ChNSs behave as a reliable intracellular thermal sensor. The intracellular relative thermal sensitivity (13% $°C^{-1}$ at 37 ºC, see **Figure 4f**) of our ChNSs is among the highest intracellular thermal sensitivities at the physiological temperature range reported for other LNThs (see **Table S1** in **Supporting Information**). An inspection of **Table S1** also reveals that in very few works the reliability of intracellular thermal sensors, proved by identical calibration curves in solution and in live cells, is demonstrated. Indeed, in many of the cases included in **Table S1** the calibration curves obtained within live cells do not match the calibration curves registered in solution or suspension. Again, the robustness of the thermal response of our ChNSs is here correlated with a minimum physical interaction between the dye/paraffin medium and cytoplasm molecules, thanks to both the physical barrier provided by the silica shell and the hydrophobic character of the dye/paraffin mixture. In addition, the thermometric parameter R_g of ChNSs under the continuous irradiation of the built-in blue LED of the microscope did not undergo significant change (**Figure 4g**). This photostability enhances the reliability of ChNSs as intracellular LNThs.

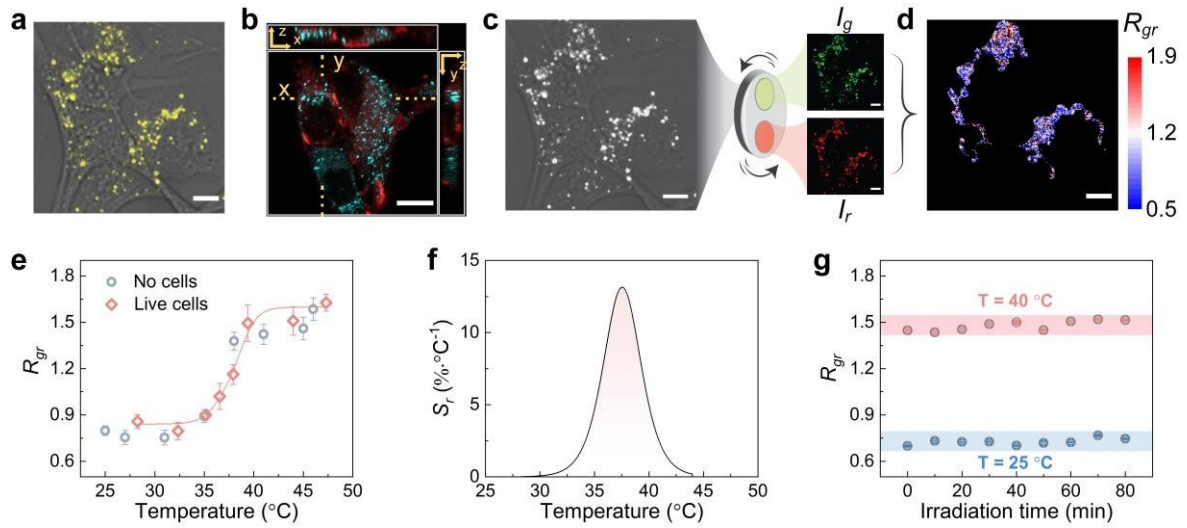

Figure 4. **(a)** Merging of the bright field and fluorescence images of live Uppsala 87 malignant glioblastoma cells incubated with ChNSs. Excitation wavelength was 415-500 nm. **(b)** Intracellular colocalization of ChNSs with CellMask stain: the red channel is CellMask stain excited by a 650 nm laser, the light blue channel is ChNSs excited by a 488 nm laser. **(c)** Schematic illustration of recording fluorescent images in two spectral ranges. Right: pseudo-color fluorescence images obtained with a 600 nm shortpass (upper) and a 600 nm longpass (lower) filters, respectively. I_g and I_r, were the average fluorescence intensities obtained from the pixels of the images. **(d)** Ratiometric image calculated from the I_g / I_r quotient. **(e)** Temperature dependence of the intensity ratio R_{gr} corresponding to ChNSs in absence of cells (no cells, gray circles) and in live cells (pink diamond). Data are presented as mean ± S.E.M. Solid line is the best fitting to a *biphasic-dose response* function. $y = 0.84 + [0.21/(1.0 + 3.0 * 10^{(36-x)})] + [0.55/(1.0 + 3.2 * 10^{(39-x)})]$, $R^2 = 0.989$. The thermal response of ChNSs is consistent in the absence and presence of cells. **(f)** Temperature dependence of the relative thermal sensitivity S_r calculated from data included in **(e).** **(g)** Time evolution of intensity ratio R_{gr} corresponding to immobilized ChNSs on a confocal dish filled with water under continuous irradiation of blue light. Data are presented as mean ± S.E.M. from n =10, n is the number of analyzed regions of interest. Scale bars: 10 μm.

2.4. Thermal monitoring of cell metabolism

Once the robustness of our ChNSs was demonstrated, we tested their potential for thermal monitoring of intracellular activity. Metabolism-induced thermal fluctuations (over the

cytoplasm volume) are typically around 1 °C on average, so exceptional care must be taken to ensure a high thermal stability in the cell population. In our experiments, the cells under

investigation were placed in a specially designed cell culture chamber that allows fine control over cell temperature and atmosphere (**Figure 5a**). A syringe pump was connected to the chamber allowing to change the composition of cell medium in a controlled way. The cell culture chamber was optically accessible allowing for real-time acquisition of fluorescence images during the modification of the medium composition. Cell metabolism was activated by the administration of 1 mL saline solution of glucose (5 mg mL^{-1}) to the cell culture medium. As soon as glucose enters the cell it undergoes glycolysis. The resulting pyruvate molecules enter mitochondria, activating cellular respiration or eventually producing lactate, hence, energy production.[28, 29] All this process is expected to increase cellular temperature after administration of glucose. To verify this, we first incubated U87-MG cells with our ChNSs. After incubation, thermal images of cells were obtained by applying the calibration curve (**Figure 4e**) to the R_{gr} images. The optical, fluorescence and ratiometric thermal images of a single cell before (basal condition) and 35 min after glucose administration are shown in **Figure 5b**. Note that this is the same cell, with its morphology changing due to cellular activity (see more details in **Figure S6**, **Supporting Information**). The temperature histograms calculated from the single-cell thermal images (**Figure 5c**) reveal how glucose administration caused an increment in the single cell average intracellular temperature ($T_{\overline{sc}}^{-}$) close to $\Delta T_{\overline{sc}}^{-}$ = + 0.9 ºC. This result is in good agreement with previously published experimental evidence: X. Di,[10] C. Gota,[17] and K. Okabe et al.[30] revealed the temperature increment induced by chemical stimulation of metabolism. O. A. Savchuk et al. employed green fluorescent protein (GFP) to measure a temperature increment in the surroundings of mitochondria close to 3 °C caused by a chemical stimulus.[31] Other works reported much larger temperature increments (up to 10 °C) but those results refer to local temperature inside the mitochondria (more details are included in **Table S1**, **Supporting Information**). In our case, we are dealing with the average temperature within the whole cell volume that it is, indeed, expected to be significantly lower than temperature changes taking place at mitochondria (where heat is generated).

To access the dynamics of cell heating caused by the activation of metabolism, we acquired thermal images of cells at different times before and after glucose administration. For each time point we determined the average temperature of the cell population being thermally imaged ($T_{\overline{cp}}^{-}$) as the average over the average temperature of individual cells, i.e. $T_{\overline{cp}}^{-} = \sum T_{\overline{sc}}^{-}/_{n}$, where n is the number of analyzed cells. $T_{\overline{cp}}^{-}$ reveals how the average cellular

temperature of the analyzed population increases due to glucose administration from basal (37.5 ºC) up to a steady- state temperature of 38.4 ºC (**Figure 5d**). This glucose-induced cell heating takes place in a

time scale of minutes. Indeed, after the administration of glucose, the $T_{\overline{cp}}$ in live cells can be fitted to an exponential growth function (dash line in **Figure 5d**) leading to a characteristic time constant of τ_h = 8 ± 3 min. In the process of glucose-induced heating there are different characteristic times involved. The time evolution of intracellular temperature after glucose administration results from a complex interplay between different dynamical processes including glucose internalization in cells, heat generation by mitochondria by glycolysis and pyruvate degradation, heat diffusion within cell, and thermal balance between cell and surrounding medium. Previous works indicated that the characteristic response time of mitochondria after a chemical stimulus (including glucose administration, see data included in **Figure S7** in **Supporting Information**) is typically of a few minutes,[32-34] which is consistent with our observations and suggests a possible mitochondrial involvement in the glucose-triggered heating process. However, the measurements of mitochondrial function over time following glucose administration revealed a significant decrease in the oxygen consumption rate (OCR) rather than an increase (**Figure 6a-b**). This finding rules out the possibility that the observed rise in temperature was due to mitochondrial activation or thermogenesis. It is well established that mitochondrial and glycolytic fluxes compensate for each other, a phenomenon known as the Warburg effect.[35] In line with this, the observed mitochondrial inhibition is associated with a slight shift towards increased glycolysis (**Figure 6c-d**), suggesting a metabolic adjustment driven by the higher availability of glucose. Notably, glycolysis is bioenergetically inefficient, yielding only 2 moles of ATP per mole of glucose, with most of the energy dissipated as cellular heat.[36, 37] Therefore, the observed glucose-triggered increase in temperature may result from a metabolic reprogramming favoring enhanced glycolysis and lactate production.

To unequivocally correlate the increment in cell temperature with the glucose-mediated activation of cell metabolism, a control experiment was performed. Glucose was added to fixed cells, i.e. in the absence of any cell activity. In this case, the administration of glucose did not induce any temperature increment, as it was expected, since glycolytic activity was suppressed (see **Figure 5d**).

The temperature histograms **(Figure 5c)** do not only evidence the intracellular glucose-induced heating but also the existence of a temperature distribution close to ± 2.0 ºC (FWHM of the temperature histograms of **Figure 5c**). Note that temperature distributions greater than 1 ºC were also observed in live cells experiments by previous researchers. For instance, K.

Okabe et al., T. Hayashi et al., R. Piñol et.al., and P. L. Silva et al. reported temperature distributions

within the cytoplasm of single cells close to ± 2.3 ºC, ± 1.8 ºC, ± 2.3 ºC, and ± 5 ºC, respectively. [30, 38-40] The temperature histograms reported in those previous works are summarized and analyzed in **Figure S8**, **Supporting Information**. The temperature distributions we found in our experiments may arise from either the inhomogeneity of intracellular temperature or the intrinsic uncertainty of our measurements. In our study, we did not observe significant difference between the width of temperature distributions obtained in presence or absence of cell activity (in both cases close to ± 2 ^{O}C, histograms of intracellular temperature obtained in live and fixed cells are compared in **Figure S9**, **Supporting Information**). Intracellular temperature is expected to be homogeneous in fixed cells, so we state that the S.D. of our thermal measurements (± 2 ^{O}C) reflects our thermal uncertainty. This fact suggests that the actual intracellular temperature inhomogeneity in our experimental conditions is smaller than the measurement accuracy (i.e. smaller than 2 ^{O}C).

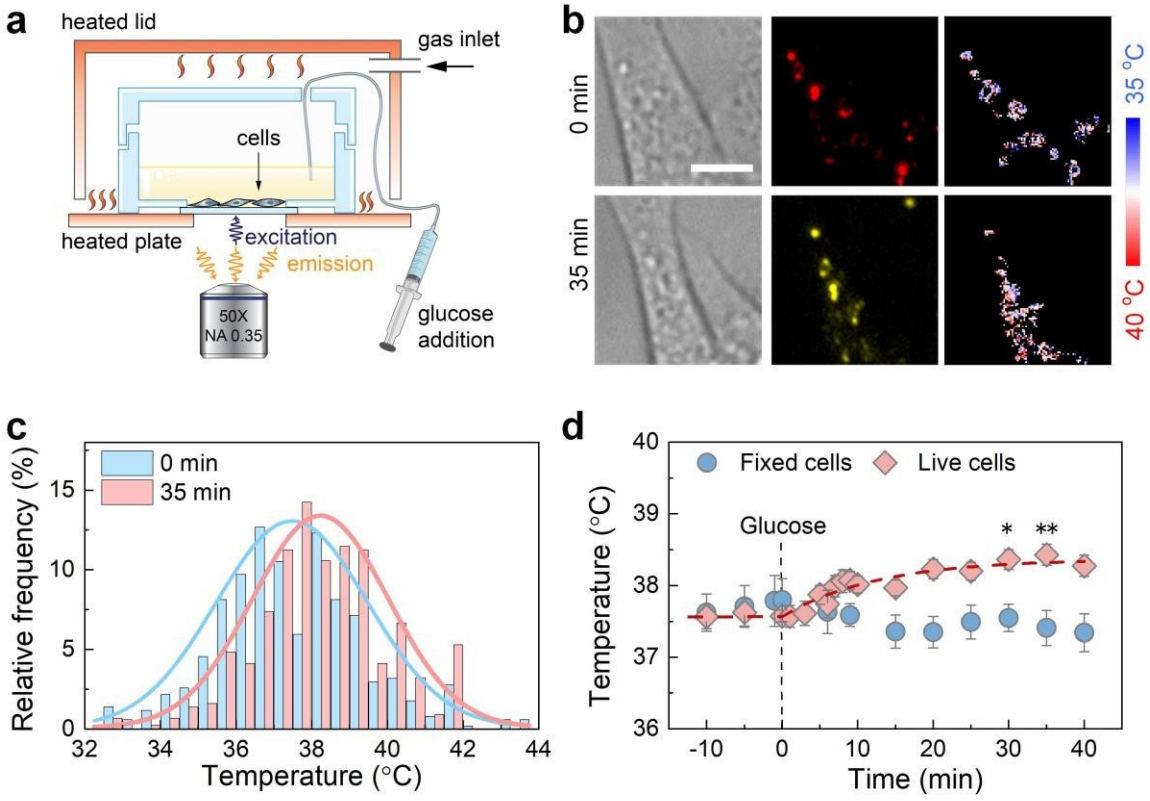

Figure 5. **(a)** Schematic representation of the experimental setup used for glucose administration to live Uppsala 87 malignant glioblastoma while simultaneously measuring their fluorescence response. The chamber was maintained at 37.5 °C, 5% CO_2 atmosphere. **(b)** Optical (left), fluorescence (middle) and thermal images (right) of individual U87-MG cell before and after the administration of glucose. Scale bar is 10 µm. **(c)** Histograms of intracellular temperature calculated from the thermal images of **(b)**. A glucose-induced temperature increment of 0.9 ºC is observed. Solid lines are the best fits to Gaussian functions.

(d) Time evolution of the intracellular temperature in live and fixed cells before and after glucose administration. Data are presented as mean ± S.E.M. from 3 replicates with n_{cell} =16. Red dash line before glucose administration indicates a constant temperature in absence of any external stimulus. Red dash line for $t > 0$ corresponds to the best fitting of experimental data to an exponential growth function. $y = 38 - 0.81 * e^{(-x/13)}$. The data obtained in fixed cells are also included showing no increase in intracellular temperature after glucose administration. Statistical significance is indicated by * and ** for $p < 0.05$ and $p < 0.01$, respectively, compared to temperature at 0 min.

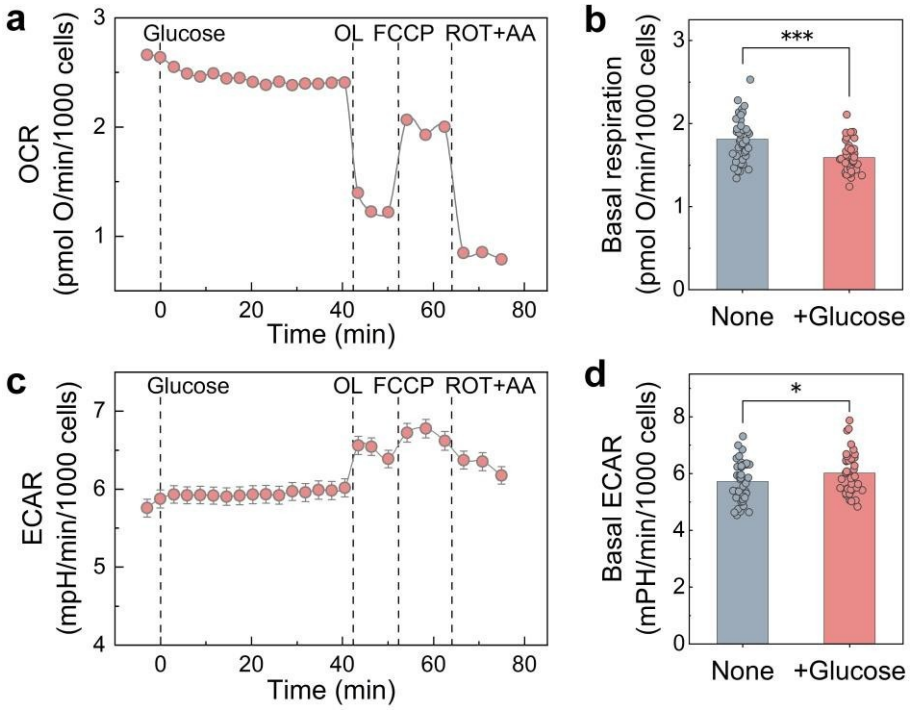

Figure 6. Representative profiles of mitochondrial respiration and glycolysis rate in U87-MG cells: **(a)** mitochondrial oxygen consumption rate (OCR) and **(c)** extracellular acidification rate (ECAR) over time. OL, oligomycin (ATP synthase inhibitor); FCCP, carbonyl cyanide 4-(trifluoromethoxy)phenylhydrazone (mitochondrial uncoupler); ROT, rotenone (mitochondrial complex I inhibitor); AA, antimycin A (mitochondrial complex III inhibitor). Bar charts show the quantification of **(b)** basal mitochondrial respiration (OCR) and **(d)** glycolytic flux (ECAR) before and after glucose administration. Data are presented as mean ± S.E.M. from $n = 25$ replicates. Statistical significance is indicated by * and *** for $p < 0.05$ and $p < 0.001$, respectively, compared to untreated cells (None).

3. Conclusion

This study presents the development and application of a novel class of fluorochromic nanothermometer (ChNSs) designed for precise intracellular temperature monitoring. This nanothermometer is based on silica nanocapsules filled with a phase-change fluorescent medium, which exhibits a complete chromatic switch in response to temperature changes within the physiological range. The phase transition-related optical properties of the encapsulated material enable a highly sensitive ratiometric analysis of intracellular temperature variations, making them ideal for detecting subtle thermal changes associated with cellular metabolism. Our results demonstrate that ChNSs maintain consistent thermal sensitivity across various biological conditions, including different pH levels, viscosities, ionic strengths, and the presence of glucose. Our ChNSs are free for crosstalk and intracellular biased sensing, ensuring their robustness and reliability in complex intracellular environments. Furthermore, the calibration of the thermal response of ChNSs in live cells matches the calibration in absence of cells, which confirms that our ChNSs are robust sensors against the intracellular physico- chemical fluctuations associated with cell activity.

We successfully applied ChNSs to monitor intracellular temperature changes during cellular metabolism activation, highlighting their potential for real-time, precise thermal imaging in biological research. The observed temperature increasement upon glucose administration validated the capability of our ChNSs to track metabolic heat production, which aligns with previous studies on intracellular thermogenesis.

The outstanding thermal sensitivity and stability of ChNSs provide a promising tool for advancing our understanding of cellular dynamics and metabolism. Future research should explore the use of these nanothermometers in more complex biological systems and investigate their application in other temperature-sensitive biological processes.

4. Experimental Section/Methods

Preparation of silica nanocapsules: The silica nanocapsules were prepared through a method adapted from the literature.[41] A mixture of PDI (6 mg), EC (50 mg), DC (50mg) and the silica precursor (methyltrimethoxyxilane, 300 mg) were added to an aqueous solution of polyvinylalcohol (20 mL, 2.5 mg mL^{-1}). The mixture was then emulsified by using ultrasonifier Branson 450 W, with 1.2 cm sonication tip. Next, the mixture pH was changed to pH = 11 to trigger the hydrolysis and polycondensation of the silica precursor, which was left to occur over 16 h. Afterwards, the nanocapsules were washed 5 times by crossflow filtration using a PES 500 kD filter, after which a suspension of ~ 5 mg mL^{-1} of nanocapsules was obtained. The

concentration of the nanocapsules was calculated for each batch from the dried content of 500 µL of the purified suspension.

Spectroscopy measurement and temperature calibration: The emission spectra were recorded by a spectrometer (QE65000, OceanOptics) for suspensions of ChNSs (0.1 mg mL^{-1}) in deionized water under 405 nm excitation. To investigate the evolution of the spectrum with temperature, a Peltier temperature controller (Q-pod 2e, Quantum Northwest) was used to control the temperature of the ChNSs being measured. All spectra were taken after up to 20 min of thermal stabilization in the 25–60 °C temperature range.

Fluorescence stability of ChNSs against environmental parameters: The spectrometer was used to measure the emission spectra of ChNSs under different pH, viscosity, K^+ ionic strength, and glucose. The buffer solutions with different pH values (5.8, 6.6, 7.4, 8) were prepared by mixing NaH_2PO_4 and NaOH in different proportions. The solution with viscosity of 1.65 cP was prepared by dissolving polyacrylamide (0.7 mg mL^{-1}) in distilled water. Different K^+ ionic strengths (120, 150, 180 mM) were obtained by adding different amounts of KCl powder in distilled water. 5 mg mL^{-1} glucose was obtained by dissolving glucose powder in distilled water. The ChNSs were added to the above prepared solution at a concentration of 0.1 mg mL^{-1}.

Cell culture and preparation: Uppsala 87 malignant glioblastoma cells were cultured in Dulbecco's modified Eagle’s medium (DMEM, Cytiva), supplemented with 10% fetal bovine serum (Cytiva) and 1% Penicillin-Streptomycin (HyClone), at 37 °C and 5% CO_2 atmosphere.

For the experiments, 35 000 cells were plated on 35 mm culture dishes with 20 mm treated glass bottom (734-2904, VWR), in a final volume of 2 mL of growing medium. For fixation, the cells were kept in 4% paraformaldehyde in Phosphate Buffered Saline (PBS) for 10 min at 37 °C. After washing with PBS for three times, the cells were kept in PBS (2 mL).

Live cell imaging and temperature calibration in cells: The U87-MG cells were incubated with ChNSs (150 μg mL-1) in the DMEM at 37 °C in the presence of 5% CO_2. After 24 h of incubation, the U87-MG cells were washed with PBS for three times and then maintained in 2 mL DMEM without red phenol. The cells incubated with ChNSs were excited by a broadband blue light, 415-500 nm (pE-300, CoolLED). The fluorescence image was collected by a camera (iXon Ultra 897 EMCCD, Andor) connected with a fluorescence microscope (ECLIPSE Ti2- U, Nikon). The exposure time of the camera was set to 2 s for recording all fluorescence images. Two spectral ranges were recorded separately by using two filters (FESH0600 and FELH0600, Thorlabs) mounted on a motorized filter wheel (switching time less than 1 s, FW102C, Thorlabs). A heating plate was used to control the temperature of the cells being measured. All images were taken after 5 min of thermal stabilization in the 28 – 47 °C temperature range.

Confocal imaging of the ChNSs in U87-MG labeled by tracking stain: Cells incubated with ChNSs (150 μg mL^{-1}) were grown on a coverslip inside a culture dish with DMEM for 24 h. After washing the cells with PBS for three times, the staining solution (C10046, CellMask™ deep red, invitrogen) was added to the dish at 37 °C for 10 min according to the supplier instructions. For fixation, the cells were washed with PBS for three times and fixed with 4% paraformaldehyde in PBS for 10 min at 37 °C. After washing, the cells were cured on the coverslip with the gold antifade reagent (P10144, ProLong™, invitrogen) for 24 h. The ChNSs internalization was verified by taking 3D confocal images (XY, XZ and YZ slices) of both the ChNSs and the stained cells.

Analysis of fluorescence images: All fluorescence images of the cells incubated with ChNSs were analyzed by using ImageJ software. Each cell in the image was selected as a region of interest. The luminescence intensity of the same region was obtained from the images recorded from the shortpass and longpass filters, respectively. The green-to-red ratio was calculated by dividing average intensities obtained from pixel-by-pixel in the same region. The images were not subjected to any modification when calculating the ratio, except that the background was subtracted prior to analysis.

Glucose Administration: The U87-MG cells incubated with ChNSs were grown on a 35 mm culture dish for 24 h with DMEM. Before glucose administration, the cells were washed with PBS for three times and then incubated with 1 mL DMEM without red phenol (4.5 mg mL^{-1} glucose) for 1.5 h. The dish was placed in a fluorescence imaging chamber connected with a gas mixer (ibiGM2-B40ibidi, ibidi) and heated lid and plate connected with a temperature controller (ibiTC2-723, ibidi). Ten minutes before glucose administration, two ratiometric images were recorded for comparison. 1 mL pre-warmed (37.5 °C) saline solution of glucose (5 mg mL^{-1}) was added into the dish through a syringe pump connected with a soft tube. The fluorescence images were recorded from the moment of glucose administration until 40 min. Experiment was performed on live and fixed cells, respectively.

Metabolic measurements by SeaHorse XFe96 analyser: The mitochondrial oxygen consumption rate (OCR) and extracellular acidification rate (ECAR) in U87-MG cells were determined using a SeaHorse XF96 analyser (Agilent) with the XFe96 Flux Pack (Agilent) following the manufacturer's protocols. In brief, 25000 cells/well were plated in DMEM without red phenol. OCR and ECAR were measured every 2 min 30 sec. The final concentration and order of injected substances was 4.75 mg mL^{-1} glucose, 1 μM oligomycin (OL), 1 μM carbonyl cyanide 4-(trifluoromethoxy)phenylhydrazone (FCCP, resulting in maximal respiration), 1 μM Rotenone and 1 μM Antimycin A (Rot + AA).

Statistical Analysis: Data are presented as mean ± S.E.M. of the indicated n and analyzed using GraphPad Prism 9 software package. For the glucose adminstration experiment, one-way analysis of variance (ANOVA) followed by Bonferroni multiple comparison *post-hoc* test was used, $n = 16$. For metabolic measurements by SeaHorse XFe96 analyser, two-tailed Student's t-test was used to compare data from two groups, $n = 25$. $p < 0.05$ was regarded as statistically significant (*$p < 0.05$, **$p < 0.01$, ***$p < 0.001$, and ****$p < 0.0001$).

Supporting Information

Acknowledgements

This work was supported by grants PID2021-127983OB-C21, PID2021-127983OB-C22, PID2022-141293OB-I00, TED2021-129937B–I00, CNS2022-135495, and PID2023-151078OB-I00 funded by MICIU/AEI/10.13039/501100011033 and by ERDF – "A way of making Europe". The ICN2 is supported by the Severo Ochoa Centres of Excellence program, Grant CEX2021-001214-S, funded by MICIU/AEI/10.13039.501100011033. UAB thanks the

support from Generalitat de Catalunya (2021 SGR 00064 project). Authors acknowledge the use of instrumentation as well as the technical advice provided by the Joint Electron Microscopy Center at ALBA (JEMCA) and funding from Grant IU16-014206 (METCAM-FIB) to ICN2 funded by the European Union through the European Regional Development Fund (ERDF), with the support of the Ministry of Research and Universities, Generalitat de Catalunya. L.F. was supported by grant PID2022-136738OB-I00 funded by MICIU/AEI/10.13039/501100011033 and by grant of Fundación Ramón Areces. S.C. was supported by grant PID2020-114054RA-I00 and CNS2023-143646 funded by MICIU/AEI/10.13039/501100011033 and European Union NextGenerationEU/PRTR. F.Z. acknowledges the scholarship from China Scholarship Council (No. 202108440235). J.R.O. thanks the Generalitat de Catalunya (AGAUR) for his predoctoral FI fellowship. M.P.O. acknowledges the financial support from MICINN for an FPU (FPU20/03166). Á.A. is grateful for his Juan de la Cierva Fellowship Grant FJC2021-047006-I funded by MCIN/AEI/10.13039/501100011033 and by the "European Union NextGeneration EU/PRTR". J.H. is a Serra Húnter Fellow. B.S.A. is supported by an FPU predoctoral grant (FPU2022/00218).

Conflict of Interest

The authors declare no conflict of interest.

Data Availability Statement

The data that support the findings of this study are available from the corresponding author upon reasonable request.

Received: ((will be filled in by the editorial staff)) Revised: ((will be filled in by the editorial staff)) Published online: ((will be filled in by the editorial staff))

References

[1] A. Bahat, I. Tur-Kaspa, A. Gakamsky, L. C. Giojalas, H. Breitbart, M. Eisenbach, *Nature Medicine* **2003**, 9, 149.
[2] D. A. Warner, R. Shine, *Nature* **2008**, 451, 566.
[3] R. S. Seymour, *Bioscience Reports* **2001**, 21, 223.
[4] R. Sakaguchi, S. Kiyonaka, Y. Mori, *Current Opinion in Biotechnology* **2015**, 31, 57.

[5] T. Bai, N. Gu, *Small* **2016**, 12, 4590.
[6] F. Wang, Y. Han, N. Gu, *ACS Sensors* **2021**, 6, 290.
[7] C. D. S. Brites, P. P. Lima, N. J. O. Silva, A. Millan, V. S. Amaral, F. Palacio, L. D. Carlos, *Nanoscale* **2012**, 4, 4799.
[8] D. Jaque, F. Vetrone, *Nanoscale* **2012**, 4, 4301.
[9] C. D. S. Brites, S. Balabhadra, L. D. Carlos, *Advanced Optical Materials* **2019**, 7, 1801239.
[10] X. Di, D. Wang, J. Zhou, L. Zhang, M. H. Stenzel, Q. P. Su, D. Jin, *Nano Letters* **2021**, 21, 1651.
[11] Y. Takei, S. Arai, A. Murata, M. Takabayashi, K. Oyama, S. i. Ishiwata, S. Takeoka, M. Suzuki, *ACS Nano* **2014**, 8, 198.
[12] Y. Gu, R. Piñol, R. Moreno-Loshuertos, C. D. S. Brites, J. Zeler, A. Martínez, G. Maurin-Pasturel, P. Fernández-Silva, J. Marco-Brualla, P. Téllez, R. Cases, R. N. Belsué, D. Bonvin, L. D. Carlos, A. Millán, *ACS Nano* **2023**, 17, 6822.
[13] T. Tsuji, K. Ikado, H. Koizumi, S. Uchiyama, K. Kajimoto, *Scientific Reports* **2017**, 7, 12889.
[14] L. Shen, T.-R. Xie, R.-Z. Yang, Y. Chen, J.-S. Kang, *Scientific Reports* **2018**, 8, 13065.

[15] P. Rodríguez-Sevilla, G. Spicer, A. Sagrera, A. P. Adam, A. Efeyan, D. Jaque, S. A. Thompson, *Advanced Optical Materials* **2023**, 11, 2201664.
[16] R. Lazarus, R. Kothari, S. Kaja, V. V. K. Venuganti, A. Nag, *Analyst* **2023**, 148, 3169.
[17] C. Gota, K. Okabe, T. Funatsu, Y. Harada, S. Uchiyama, *Journal of the American Chemical Society* **2009**, 131, 2766.
[18] J. Zhou, B. del Rosal, D. Jaque, S. Uchiyama, D. Jin, *Nature Methods* **2020**, 17, 967.
[19] A. H. Johnstone, *CRC Handbook of Chemistry and Physics—69th Edition Editor in Chief R. C. Weast, CRC Press Inc., Boca Raton, Florida, 1988, pp. 2400, price £57.50. ISBN 0–8493–0369–5*, **1991**.
[20] J. R. Otaegui, D. Ruiz-Molina, L. Latterini, J. Hernando, C. Roscini, *Materials Horizons* **2021**, 8, 3043.
[21] J. R. Otaegui, A. Carrascull-Marín, D. Ruiz-Molina, J. Hernando, C. Roscini, *Advanced Optical Materials* **2022**, 10, 2200083.
[22] J. R. Otaegui, D. Ruiz-Molina, J. Hernando, C. Roscini, *Advanced Functional Materials* **2024**, 34, 2402510.
[23] K. Xue, S. Huang, K. Wu, Z. Sun, H. Fu, C. Wang, C. Wang, C. Zhu, *Anal. Chem.* **2024**, 96, 11026.
[24] R. Sens, K. H. Drexhage, *Journal of Luminescence* **1981**, 24-25, 709.
[25] T. P. van Swieten, A. Meijerink, F. T. Rabouw, *ACS Photonics* **2022**, 9, 1366.
[26] T. Zhao, K. Asawa, T. Masuda, A. Honda, K. Kushiro, H. Cabral, M. Takai, *Journal of Colloid and Interface Science* **2021**, 601, 825.
[27] N. Xie, J. Huang, X. Yang, X. He, J. Liu, J. Huang, H. Fang, K. Wang, *Analytical Chemistry* **2017**, 89, 12115.
[28] M. G. Vander Heiden, L. C. Cantley, C. B. Thompson, *Science* **2009**, 324, 1029.
[29] F. Beignon, N. Gueguen, H. Tricoire-Leignel, C. Mattei, G. Lenaers, *Cellular and Molecular Life Sciences* **2022**, 79, 525.
[30] K. Okabe, N. Inada, C. Gota, Y. Harada, T. Funatsu, S. Uchiyama, *Nat. Commun.* **2012**, 3, 705.
[31] O. A. Savchuk, O. F. Silvestre, R. M. R. Adão, J. B. Nieder, *Scientific Reports* **2019**, 9, 7535.
[32] B. Tan, H. Xiao, F. Li, L. Zeng, Y. Yin, *Animal Nutrition* **2015**, 1, 239.
[33] X. Gu, Y. Ma, Y. Liu, Q. Wan, *STAR Protocols* **2021**, 2, 100245.
[34] H. Zhang, J. Tang, Y. Cao, T. Wang, *Evidence-Based Complementary and Alternative Medicine* **2022**, 2022, 9302403.
[35] R. J. DeBerardinis, N. S. Chandel, *Nature Metabolism* **2020**, 2, 127.
[36] C. B. Scott, *Nutrition & Metabolism* **2005**, 2, 14.
[37] S. MINAKAMI, C.-H. de VERDIER, *European Journal of Biochemistry* **1976**, 65, 451.
[38] T. Hayashi, N. Fukuda, S. Uchiyama, N. Inada, *PLOS ONE* **2015**, 10, e0117677.
[39] R. Piñol, J. Zeler, C. D. S. Brites, Y. Gu, P. Téllez, A. N. Carneiro Neto, T. E. da Silva, R. Moreno-Loshuertos, P. Fernandez-Silva, A. I. Gallego, L. Martinez-Lostao, A. Martínez, L. D. Carlos, A. Millán, *Nano Letters* **2020**, 20, 6466.
[40] P. L. Silva, O. A. Savchuk, J. Gallo, L. García-Hevia, M. Bañobre-López, J. B. Nieder, *Nanoscale* **2020**, 12, 21647.
[41] H. Zhang, X. Wang, D. Wu, *J. Colloid Interface Sci.* **2010**, 343, 246.

Table of contents

A chromatic nanoswitcher for thermal monitoring of cell metabolism

Fengchan Zhang, Marina París Ogáyar, Álvaro Artiga, Jordi Hernando, Eva Villar-Álvarez, Julia Lorenzo, Beñat Salegi Ansa, Sara Cogliati, Laura Formentini, Patricia Haro-González, Daniel Ruiz-Molina, Jaume Ramon Otaegui,* Claudio Roscini,* and Daniel Jaque*

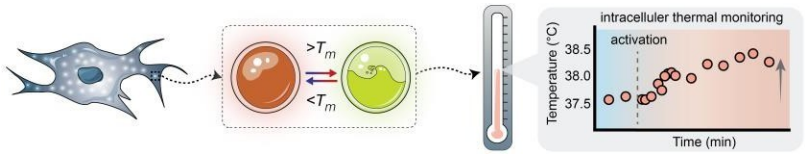

This study presents a novel class of luminescent nanothermometer, chromatic nanoswitcher (ChNS), designed for precise intracellular temperature monitoring. The phase transition-related optical properties of ChNS enable a highly thermal sensitive in the physical temperature range with a thermal response independent by fluctuations of other physiological factors like pH, viscosity or ionic strength. We successfully applied ChNS to achieve intracellular thermal monitoring of cellular metabolism.